metals

MDPI

Article

Post-Rolling Cooling Phase Transformation and Microstructure of High-Strength Anti-Seismic Rebars with Different Solute Nb and Austenite Microstructure

Xing Liu [1], Jianchun Cao [1,*], Wei Chen [2], Weiqiang Zhang [2], Yongqing Zhang [3], Shubiao Yin [4] and Aimin Guo [3]

[1] Faculty of Materials Science and Engineering, Kunming University of Science and Technology, Kunming 650093, China
[2] WISCO (Wuhan Iron and Steel Corporation) Kunming Iron and Steel Co., Ltd. (KISC), Kunming 650302, China
[3] CITIC Metal Microalloying Technical Center, Beijing 100004, China
[4] Faculty of Metallurgy and Energy Engineering, Kunming University of Science and Technology, Kunming 650093, China
* Correspondence: nmcjc@163.com

Abstract: Three types of 20MnSiNb high-strength anti-seismic steels with different solute niobium and austenite microstructural characteristics were obtained through thermal simulation experiments which involved changing the reheating temperature and finish-rolling temperature; the dynamic CCT curve, microstructure transformation, precipitates and hardness of the steels were also studied. The results show that the ability of solute Nb to refine austenite grains is stronger than that of undissolved Nb. Lowering the reheating temperature and finish-rolling temperature can refine the prior austenite microstructure and keep the deformed austenite after hot rolling, respectively, and make the dynamic CCT curve move to the upper left, which promotes the formation of proeutectoid ferrite and pearlite, and inhibits the formation of bainite at low cooling rates. The increase in solute Nb and the deformed austenite grains effectively promote the precipitation of Nb-containing precipitates during the cooling process after rolling, and improve the precipitation strengthening effect of Nb. This research provides a theoretical basis for the production of Nb microalloyed high-strength anti-seismic rebars.

Keywords: niobium; austenite; high-strength anti-seismic rebar; dynamic CCT

Citation: Liu, X.; Cao, J.; Chen, W.; Zhang, W.; Zhang, Y.; Yin, S.; Guo, A. Post-Rolling Cooling Phase Transformation and Microstructure of High-Strength Anti-Seismic Rebars with Different Solute Nb and Austenite Microstructure. *Metals* **2022**, *12*, 1734. https://doi.org/10.3390/met12101734

Academic Editor: Andrey Belyakov

Received: 22 September 2022
Accepted: 12 October 2022
Published: 16 October 2022

1. Introduction

With the rapid development of the construction industry, the problem of earthquake resistance has also attracted widespread attention, so the complex structures of large public buildings, high-rise buildings and other buildings have increasingly higher requirements on the carrying capacity of rebars [1–4]. High-strength hot-rolled ribbed rebars of 400 MPa grade and above have high strength, stable performance, large safety reserves and good anti-seismic properties, which are more suitable for high-rise large-span and anti-seismic building structures [4–8]. At present, the main construction steel is hot-rolled 20MnSi ribbed steel, which is mainly produced by microalloying technology, ultra-fine grain technology or residual heat treatment process [9–14]. However, according to the new standard GB1499.2-2018 of hot-rolled ribbed rebars of China, the edge microstructure cannot be closed-loop martensite, and requires a uniform ferrite + pearlite (F+P) microstructure from the inside to the outside. Therefore, in order to ensure the uniformity of internal and external microstructure of rebars, it is necessary to use microalloying technology for production [13,14], in which niobium microalloying and vanadium microalloying are the main production technologies.

Compared with vanadium microalloying technology [3,15–17], high-strength anti-seismic rebars produced by niobium microalloying technology [18–20] have a higher tensile-to-yield ratio, and the price of ferroniobium has been stable for a long time, which

helps the factory to control costs. Therefore, Niobium microalloying technology has attracted extensive attention from a large number of researchers and producers. Since the solid solubility product of niobium carbonitrides in austenite is lower than that of vanadium carbonitrides, the production of Nb-containing steel requires a higher reheating temperature (RT), so that Nb can be dissolved in austenite as much as possible, and the precipitation strengthening and fine-grain strengthening of Nb can be fully exerted. However, the previous research of our group [20] shows that adding niobium element to 20MnSi steel enhances the stability of supercooled austenite, significantly promotes the formation of bainite, and moves the bainite transformation range in the CCT curve to the right. The existence of bainite microstructures in steel will significantly affect properties of high-strength anti-resistant rebars. Zeng's [21] studies have shown that when the content of Nb in high-strength anti-seismic rebars reaches 0.035% to 0.060%, a large number of bainite microstructures will appear, resulting in rebars with high tensile strength but no yield phenomenon. The research results of Chen [22] on niobium show that the high reheating temperature will make the prior austenite grains more coarse, and promote the formation of bainite. The brittleness of the rebar increases, the elongation decreases, and the brittle fracture occurs when the bainite content reaches 50%.

The form of existence of Nb and the austenite microstructure characteristics are important factors that affect the cooling transformation and microstructure of high-strength rebars after rolling. However, the investigations about the effects of Nb and prior austenite on the microstructure transformation and properties of high-strength anti-seismic rebars are lacking. In this paper, the post-rolling cooling phase transformation and microstructure of high-strength anti-seismic rebars with different solute Nb and austenite microstructures by changing different reheating and finish-rolling temperature (FRT) were studied. The purpose is to lay a theoretical foundation for the production practice of Nb-microalloyed high-strength anti-seismic rebars.

2. Materials and Methods

We used 20MnSiNb steel in the present investigation, which had the following chemical composition: Fe-0.22C-0.38Si-1.14Mn-0.017S-0.038P-0.0062N-0.030Nb (wt%), which was provided by a domestic steel plant (Kunming Iron and Steel Co., Ltd., Kunming, China). The thermal simulation experiments were carried out with a THERMECMASTER-Z machine (Fuji Radio Machinery Co., Ltd, Fuji, Japan) to analyze the influence of the solute Nb and austenite microstructures on the phase transformation after rolling. The cylindrical specimens, 8 mm in diameter and 12 mm in length, were processed by lathe and prepared for the thermal simulation experiments.

In order to obtain samples with different solute Nb and austenite microstructural characteristics, the method of changing reheating temperature and finish-rolling temperature was adopted. Figure 1 shows the three thermal simulation experiment process, where ε refers to the strain rate and *D* is pass reduction. The tested steels were subjected to thermal simulation experiments in sequence according to different processes, which were named as Nb-1, Nb-2, and Nb-3.

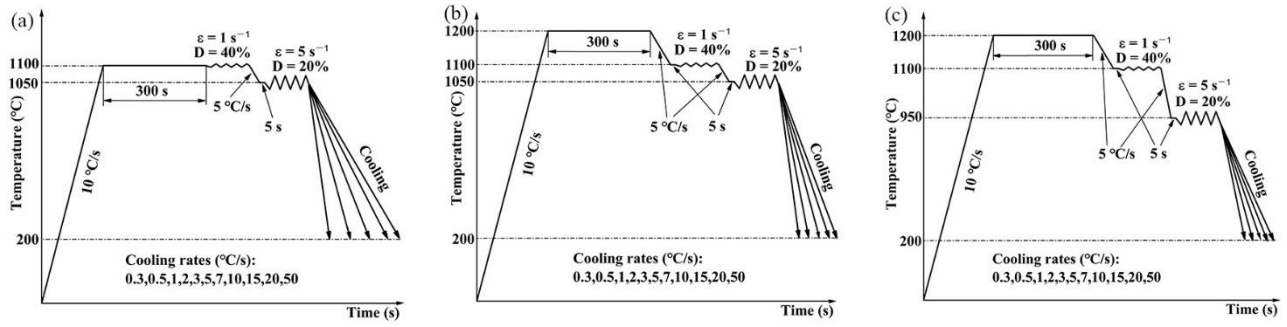

Figure 1. Thermal simulation experiment process of (**a**) Nb-1, (**b**) Nb-2, (**c**) Nb-3.

The tested steel was first heated to 1100 °C and 1200 °C, respectively, and held for 300 s, and then quenched to room temperature to observe the prior austenite grains and undissolved phases, as shown in Figure 2a–d.

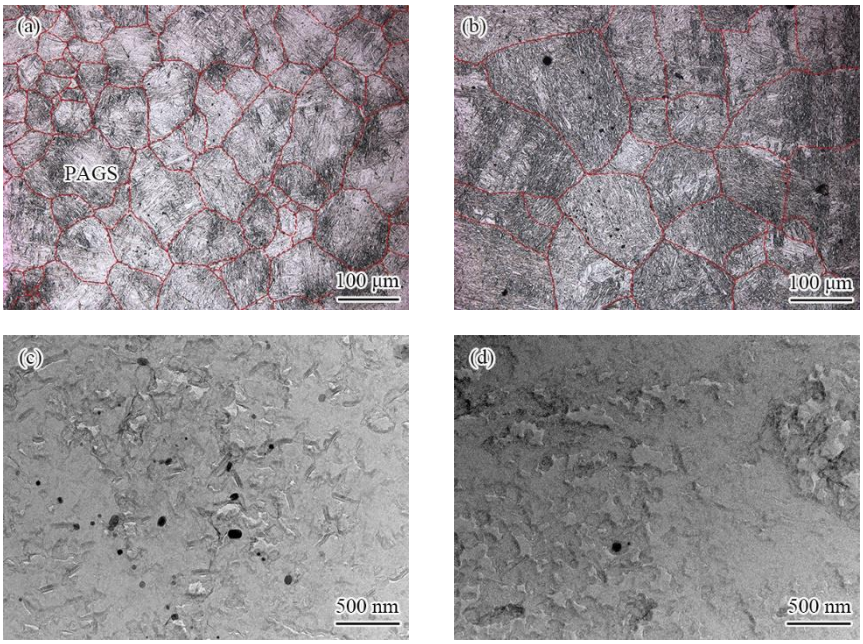

Figure 2. Prior austenite grains and undissolved phase at (**a**,**c**) 1100 °C and (**b**,**d**) 1200 °C.

When the RT is 1100 °C, the prior austenite grains are fine and uniform, with a size of 64.84 μm, but there are many undissolved particles, as shown in Figure 2c. However, when the RT rises to 1200 °C, the prior austenite grain becomes significantly coarser, and the average grain size is 138.63 μm, which is twice as large as the grain size of the prior austenite at 1100 °C; the undissolved phase also decreases significantly. According to study [19], the solubility product equations of two commonly used niobium carbonitrides in austenite are shown in Equations (1) and (2):

$$\lg\left\{w(\mathrm{Nb})\left[w(\mathrm{C})+\frac{12}{14}w(\mathrm{N})\right]\right\}=-\frac{8800}{T}+3.97 \quad (1)$$

$$\lg\left\{w(\mathrm{Nb})\left[w(\mathrm{C})+\frac{12}{14}w(\mathrm{N})\right]\right\}=-\frac{6770}{T}+2.26 \quad (2)$$

where: w(Nb), w(C), w(N) are mass fractions of Nb, C, N elements dissolved in matrix; T is the reheating temperature.

The equation for the Nb (C, N) solid solubility product at 1100 °C is applied to Equation (1), and Equation (2) is applied at 1200 °C. The calculation result shows that the solid solubility values of the Nb (C, N) at 1100 °C and 1200 °C are 0.016% and 0.021%, respectively.

Secondly, the tested steel after thermal simulation rolling by different processes is quenched immediately, the high-temperature microstructure after rolling is retained, as shown in Figure 3. Nb-1 steel and Nb-2 steel have the same FRT, the austenite grain morphology is equiaxed (as shown in Figure 3a,b), and average austenite grain sizes are 24.26 μm and 30.87 μm, respectively. The morphology of deformed austenite grains in Nb-3 steel is generally pancaked, as shown in Figure 3c. The average austenite grain size of Nb-3 steel is bigger than that of Nb-2 steel.

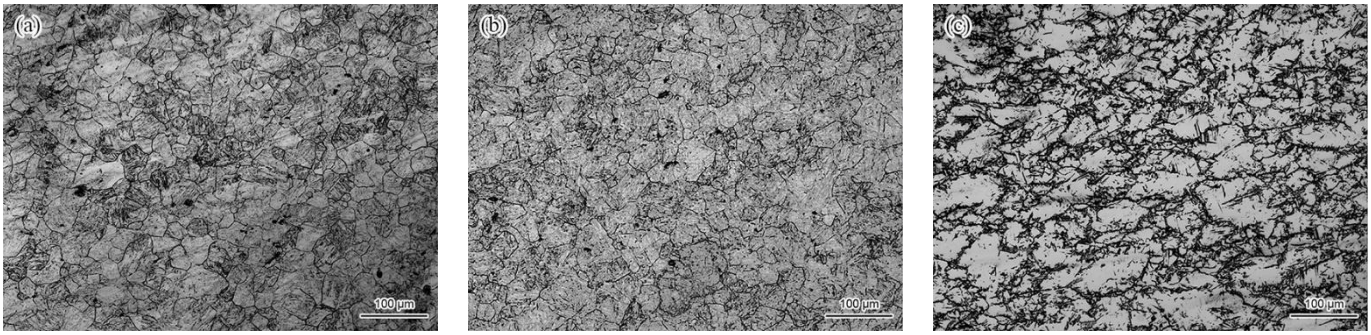

Figure 3. Austenite grain morphology with different steels of (**a**) Nb-1, (**b**) Nb-2 and (**c**) Nb-3.

Based on the YB/T 5128-93 standard, the CCT curves of Nb-microalloyed steel were drawn at three different thermal simulation experiment process in this paper. This paper used a combination of the expansion method, metallographic method and hardness method to draw the CCT curves. According to the position of the inflection point on the expansion curve and the result of microstructure inspection, the type of each transformation can be determined. Then, the tangent method was used to determine the critical point of each transition, and the OriginLab2022b software (Northampton, Massachusetts, USA) was used to plot the test results to get the CCT curve under this condition. The tested steel was heated at 0.05 °C/s to 950 °C by Formastor-F II automatic phase change measuring device (Fuji Radio Machinery Co., Ltd, Fuji, Japan). A_{c1} and A_{c3} temperatures were determined according to the linear expansion curve in the heating process. The tested steel heated to 950 °C was held for 5 min and then rapidly cooled to room temperature. The M_s temperature was determined according to the linear expansion curve in the cooling process. The Gleeble-3800 thermal simulation tester (DSI, Minnesota, USA) was used to tested cylindrical specimens of φ8 × 12 mm, simulating double pass rolling to obtain stress-strain curves under different processes, with the process referring to the rolling process of CCT experiments.

All specimens were sectioned along the longitudinal compression axis, ground and polished. The continuous specimens were etched with newly prepared 4% nitric acid solution after testing. A Leica metallographic microscope (Leica Microsystems CMS GmbH, Weizner, Germany) equipped with digital imaging facility was used for this purpose and the specific microstructure was studied by Scanning Electron Microscope (SEM) (Shanghai Yongke Optical Instrument Co., Ltd., Shanghai, China). Vicker hardness measurements were carried out on the polished samples to study the influence of different CRs by using SCTMC sclerometer (SCTMC, Shanghai, China), whose load was 10 kg and the loading time was 15 s. In the HRTEM device of model Tecnai G2 TF30 (FEI, Portland, USA), the method of extraction and replication is adopted to analyze the precipitates of the tested steel under the different cooling rates (CRs).

3. Results

3.1. Dynamic CCT Diagrams

Figure 4 presents the dynamic CCT diagrams of the tested steels. In these diagrams, "A", "F", "P", "B" and "M" are denoted austenite, ferrite, pearlite, bainite, and martensite, respectively. The measured A_{c1}, A_{c3} and M_s temperatures for the 20MnSiNb tested steels are: A_{c1} = 715 °C, A_{c3} = 835 °C and M_s = 395 °C. Representative cooling curves, cooling rates, and transformation ranges of the transformation products after continuous cooling are shown in the diagrams. As shown in Figure 4, the same types of transformation occurred in both sets of simulation at the different process, such as A → F transformation, A → P transformation, A → B transformation and A → M transformation. For ferritic transformation, the critical CR of Nb-1 steel is 7 °C/s, and the critical CR of Nb-2 steel is the same as that of Nb-3 steel, which is lower than 5 °C/s. For pearlite transformation, the CR range of Nb-1 steel is 0.3 to 3 °C/s, and the CR range of Nb-2 steel is narrower than

that of Nb-1 steel, which is 0.3 to 2 °C/s. Nb-3 steel has the same pearlite transformation CR range as Nb-1 steel. For the bainite transformation, the maximum CR of the three steels does not exceed 20 °C/s. The minimum critical CR of bainite transformation in Nb-1 steel is 2 °C/s and that of the Nb-2 steel is expanded to 0.3 °C/s, and the bainite transformation range is significantly increased when the austenite grains are coarse. When the deformed austenite grains exist, the CR of the bainite critical transformation of Nb-3 steel is 1 °C/s. For martensitic transformation, all steels have the same CR range: 7 to 50 °C/s.

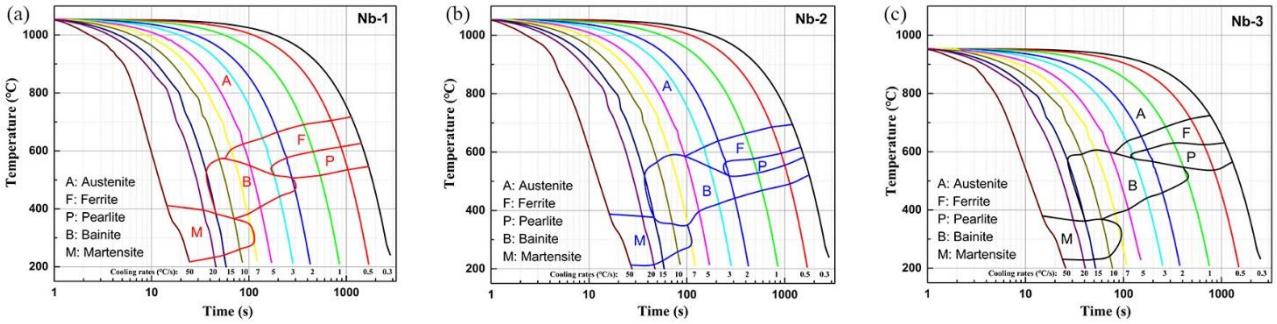

Figure 4. Dynamic CCT curve of (**a**) Nb-1, (**b**) Nb-2 and (**c**) Nb-3.

Figure 5 shows a comparison chart of different phase transformation intervals, and each microstructure transformation has a clear temperature interval. Figure 6 shows the variation in A_{r3} temperature with CR for different tested steels. Figure 5a is a comparison diagram of the phase transition interval of Nb-1 steel and Nb-2 steel under different CRs, and the RT of the two are 1100 °C and 1200 °C, respectively. With the increase in RT, the content of solute Nb and the prior austenite grains were coarse, so that the stability of the supercooled austenite increased. The dynamic CCT diagram moves to the lower right. The transformation onset temperature of proeutectoid ferrite (A_{r3}) is decreased by about 20°C. The starting temperature of pearlite transformation decreases and the final temperature increases, which obviously leads to the shrinkage of the pearlite transformation zone. The bainite transformation region has the most obvious expansion. Under the same CR, the starting temperature of bainite transformation increases and the final temperature decreases, resulting in an enlarged temperature range. Bainite transformation can be occurred in the lower cooling rates range. As can be seen above, in the Nb-microalloyed steel, coarsening of prior austenite grains can inhibit diffusion-type transformation such as ferrite and pearlite, and promote bainite transformation.

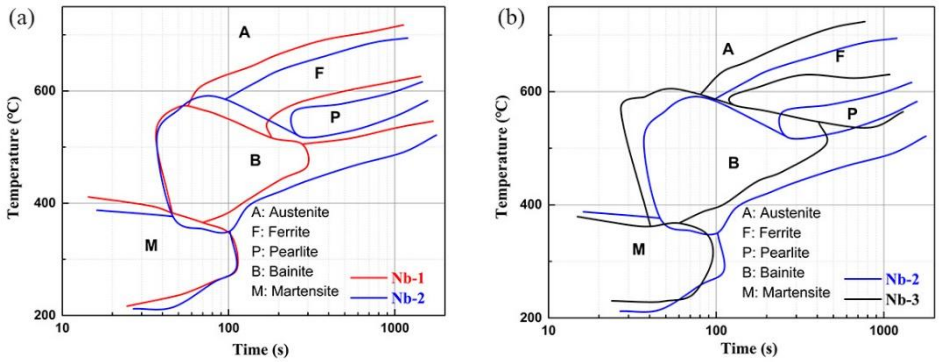

Figure 5. Comparison of different phase transformation intervals.

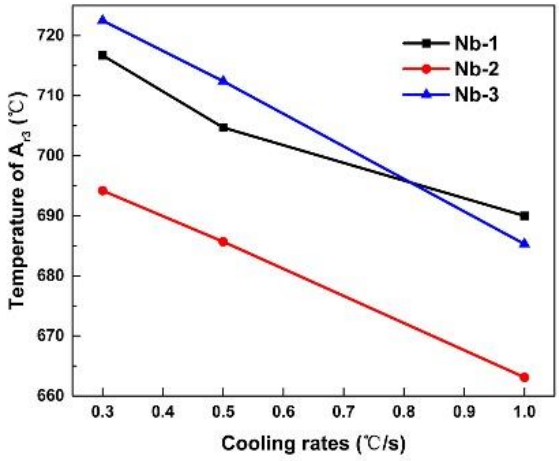

Figure 6. Dependence of A_{r3} on cooling rate of the tested steels.

Figure 5b shows a comparison of the phase transformation range of Nb-2 steel and Nb-3 steel with FRT of 1050 °C and 950 °C, respectively. The A_{r3} temperature is increased by about 30 °C, when the FRT is reduced from 1050 °C to 950 °C. The dynamic CCT diagram moves to the upper left, returning to the phase transformation range equivalent to that of Nb-1 steel. The starting temperature of pearlite transformation increases significantly, which expands the range of pearlite transformation. The critical CR of bainite transformation increases from 0.3 °C/s to 1 °C/s, and the bainite transformation range shrinks. Therefore, in Nb-microalloyed steels, deformed austenite grains can promote the occurrence of diffusive transformation and delay semi-diffusion transformation, such as in the bainite microstructure.

3.2. Microstructure

A uniform F + P microstructure from the inside to the outside of high-strength anti-seismic rebars was required according to the standard GB1499.2-2018. Figure 7 shows the metallographic microstructure of three tested steels under the CR range of 0.3 to 1 °C/s. For Nb-1 steel with fine prior austenite grains, there is always microstructure of F+P under the range of 0.3 to 1 °C/s as shown in Figure 7a–c. However, for the Nb-2 steel, when the RT rises to 1200 °C, the grain size of prior austenite becomes larger and the content of solute Nb increases, which promotes bainite transformation at low CRs (Figure 7d–f). When the FRT is reduced to 950 °C, resulting in deformed austenite grains, the complete F+P microstructure can be obtained for Nb-3 steel at low CRs (Figure 7g–h).

For Nb-1 steel with fine prior austenite grains, the shape of ferrite does not change significantly under the range of 0.3 to 1 °C/s. When the RT increases to 1200 °C, for Nb-2 steel, the formation of proeutectoid ferrite along the grain boundaries increases due to the coarsening of the prior austenite grains, as shown in Figure 7e-f. From the comparison of Nb-2 steel and Nb-3 steel, the presence of deformed austenite grains at lower CR reduces the amount of pre-eutectoid ferrite formed along the grain boundaries in Nb-3 steel. The changes in the average grain size and volume percentage of ferrite under the range of 0.3 to 1 °C/s are shown in Figure 8. The average grain size of ferrite in Nb-2 steel is larger than that of Nb-1 steel and Nb-3 steel, but the volume percentage of ferrite is the lowest. The average grain size and volume percentage of ferrite in Nb-1 steel and Nb-3 steel have little difference. Compared with Nb-2 steel, there are deformed austenite grains in Nb-3 steel, which can effectively refine the ferrite grain size, promote ferrite transformation, and increase the content of ferrite.

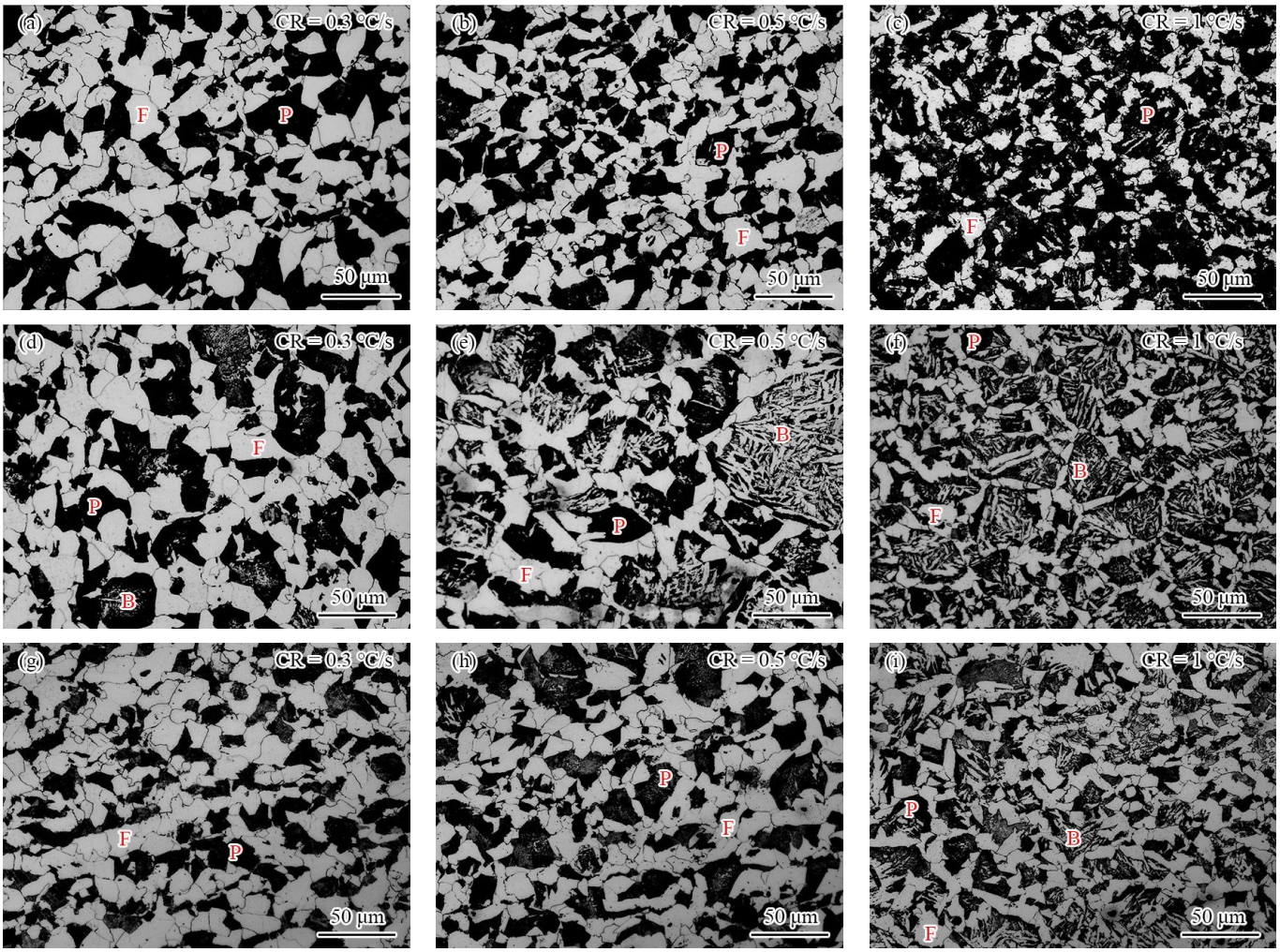

Figure 7. Microstructures of continuously-cooled specimens. (**a**–**c**) Nb-1, (**d**–**f**) Nb-2 and (**g**–**i**) Nb-3. "F", "P" and "B" are denoted ferrite, pearlite and bainite, respectively.

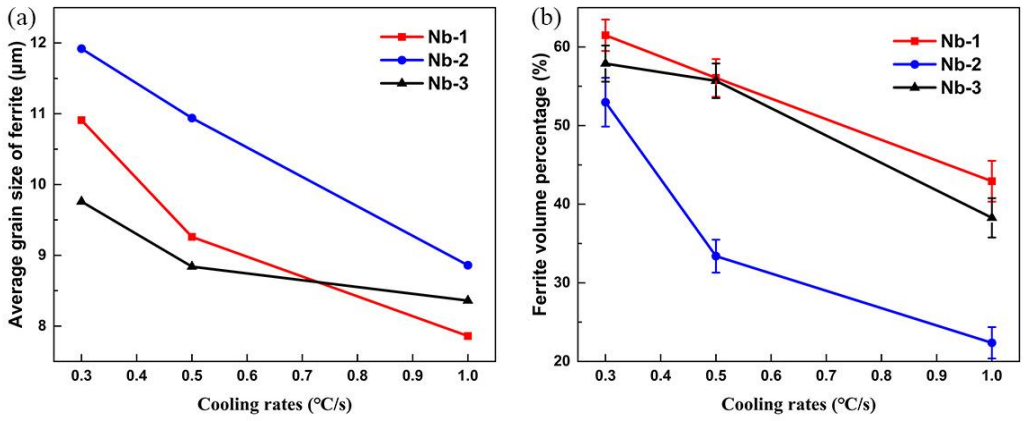

Figure 8. (**a**) Average grain size and (**b**) percentage of ferrite.

As the CR increases, the volume percentage of ferrite decreases and that of pearlite or bainite increases. Figure 9 shows a SEM micrograph of the pearlite or bainite microstructure in different tested steels under the CR range of 0.3 to 1 °C/s. As shown in Figure 9a–c, the matrix is composed of ferrite + pearlite, and the pearlite microstructure in Nb-1 steel can maintain an obvious lamellar structure under different CRs. As the CR increases, the

pearlite microstructure in Nb-1 steel degenerates and the aspect ratio is diminished. When the prior austenite grains size becomes coarser, a large amount of bainite has been formed in Nb-2 steel and mixed with the pearlite, and microstructures are F+P+B as shown in Figure 9d–f. The pearlite cluster becomes smaller, but the aspect ratio does not change much in Nb-2 steel. For the Nb-3 steel, the aspect ratio of the pearlite lath decreases with the CR increasing. Compared with Nb-1 steel, the cementite lath of Nb-3 steel is seriously degraded, and the short rod-shaped cementite is increased. Under a CR of 0.5 °C/s, as shown in Figure 9h, less bainite exists inside the pearlite, so the bainite transformation does not appear in the expansion curve. When the CR is 1 °C/s, a large amount of bainite was formed.

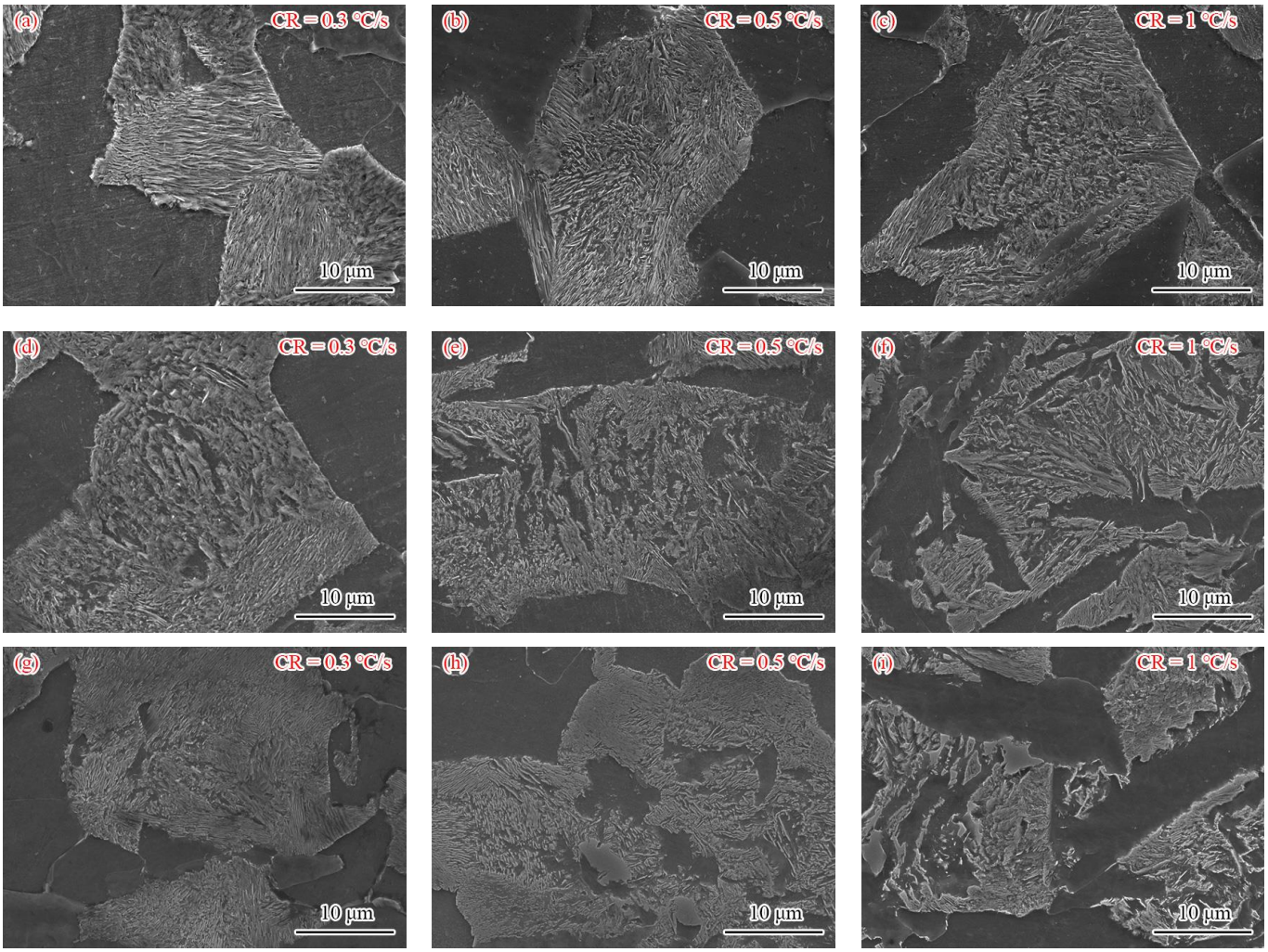

Figure 9. SEM morphologies of continuously-cooled specimens. (**a**–**c**) Nb-1, (**d**–**f**) Nb-2 and (**g**–**i**) Nb-3.

3.3. Precipitates

Figure 10 shows the TEM morphology of precipitate particles, which show that its shape tends to be pie-like. EDS analysis (Figure 10b) shows that the precipitated phase is NbC (the peak of Cu in EDS was from Cu network). Figure 10c shows the Fourier transition diagram of the precipitated phase and its calibration. The precipitate was calibrated, whose crystal band axis was [0 0 4] and the lattice constant was 0.4444 nm. The lattice constants of NbC and NbN [23,24] are 0.4470 nm and 0.4388 nm, respectively. The lattice constants of the analyzed precipitates are between those of NbC and NbN, so the Nb (C, N) with a *MC*-type precipitate can be obtained.

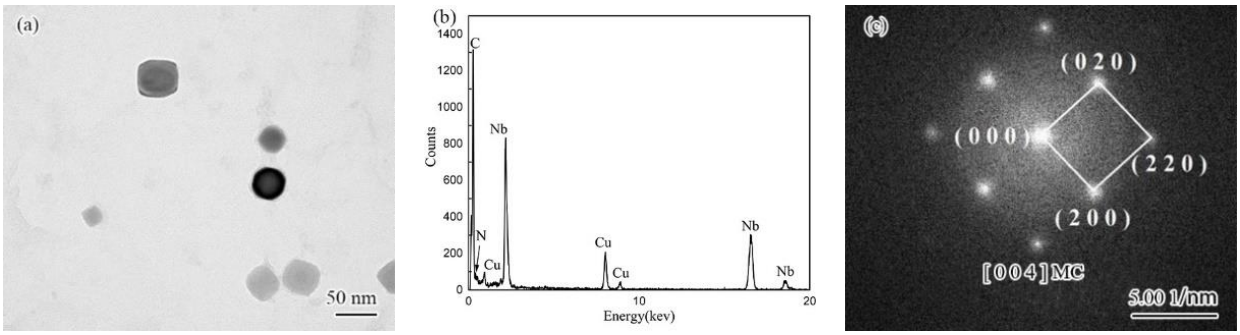

Figure 10. (**a**) TEM image of a MC-type particle precipitated, corresponding (**b**) EDS and its (**c**) FFT result.

Figure 11 shows STEM morphology of the precipitates in three tested steels at different CRs. With the decrease in CRs, the fine precipitates of three tested steels increased, and the amount of the precipitates also increased. Under CRs of 0.3 to 1 °C/s, the precipitation in Nb-2 steel is always the most, followed by Nb-3 steel, and Nb-1 steel has the least precipitation. The average size of the precipitates in Nb-2 steel is always smaller than that in Nb-1 steel at the same CR. For example, at the CR of 0.3 °C/s, the average particle sizes of the precipitates in Nb-2 steel and Nb-1 steel are 19.09 nm and 28.66 nm, respectively. Interestingly, at lower cooling rates (e.g., 0.3, 0.5 °C/s), the segregation of the second phase is always reached in pearlite, whereas in ferrite, the second phase is always precipitated along the grain boundaries. As shown in Figure 10, there are many larger particles present. Except for a small part of the undissolved phase, the rest are deformation-induced precipitates. Comparing the deformation-induced precipitates in the three tested steels, the amount of precipitates is in the order of Nb-3 steel, Nb-2 steel and Nb-1 steel. In the high temperature austenite stage, the more Nb is in the solid solution, the more favorable it is for deformation-induced precipitation.

3.4. Hardness

Figure 12 shows the variation in the hardness of the three tested steels with CRs under the range of 0.3~1 °C/s. As the CR increases, the hardness of the tested steels always increases. Under the same CR, the hardness of Nb-2 steel is always the largest, followed by Nb-3 steel, and the hardness of Nb-1 steel is the lowest. When the CR is 1 °C/s, the hardness difference between Nb-2 steel and Nb-3 steel is small. Therefore, the increase in solute Nb and the existence of deformed austenite can increase the hardness of microstructures after continuous cooling transformation.

Under the range CR of 0.3 to 1 °C/s, the ferrite grain size of Nb-2 steel is always the largest, and the effect of fine grain strengthening is weak. However, the ferrite content is low, and the bainite content increases significantly with the increase in CR. Bainite contains a large number of dislocations [25], with strong dislocation strengthening. The special existence of acicular ferrite in bainite has a significant effect on the splitting of the matrix, and has a strong fine-grain strengthening. Under different CRs, the precipitation of the second phase in Nb-2 steel is always the most, and the strengthening effect of the second phase is obvious. Therefore, the hardness of Nb-2 steel is the largest. Although the average ferrite grain size of Nb-1 steel is smaller than that of Nb-2 steel, the proportion of ferrite in Nb-1 steel is higher. The ferrite is a soft and ductile phase, and its strength is relatively low. In addition, the Nb-containing precipitates are less. Therefore, the hardness of Nb-1 steel is the lowest. Similar with Nb-1 steel, Nb-3 steel has a higher proportion of ferrite, and the precipitation of the second phase is less than that of Nb-2 steel. Bainite only appears when the CR is 1 °C/s, and the content is small. To sum up, the microhardness in Nb-3 steel is between that of Nb-1 steel and Nb-2 steel. Pavlina [26] summarized a large number of

experimental data and obtained the empirical relationship between yield strength, tensile strength and hardness as follows:

$$YS = -90.7 + 2.876H_{\mathrm{v}} \tag{3}$$

$$TS = -99.9 + 3.734H_{\mathrm{v}} \tag{4}$$

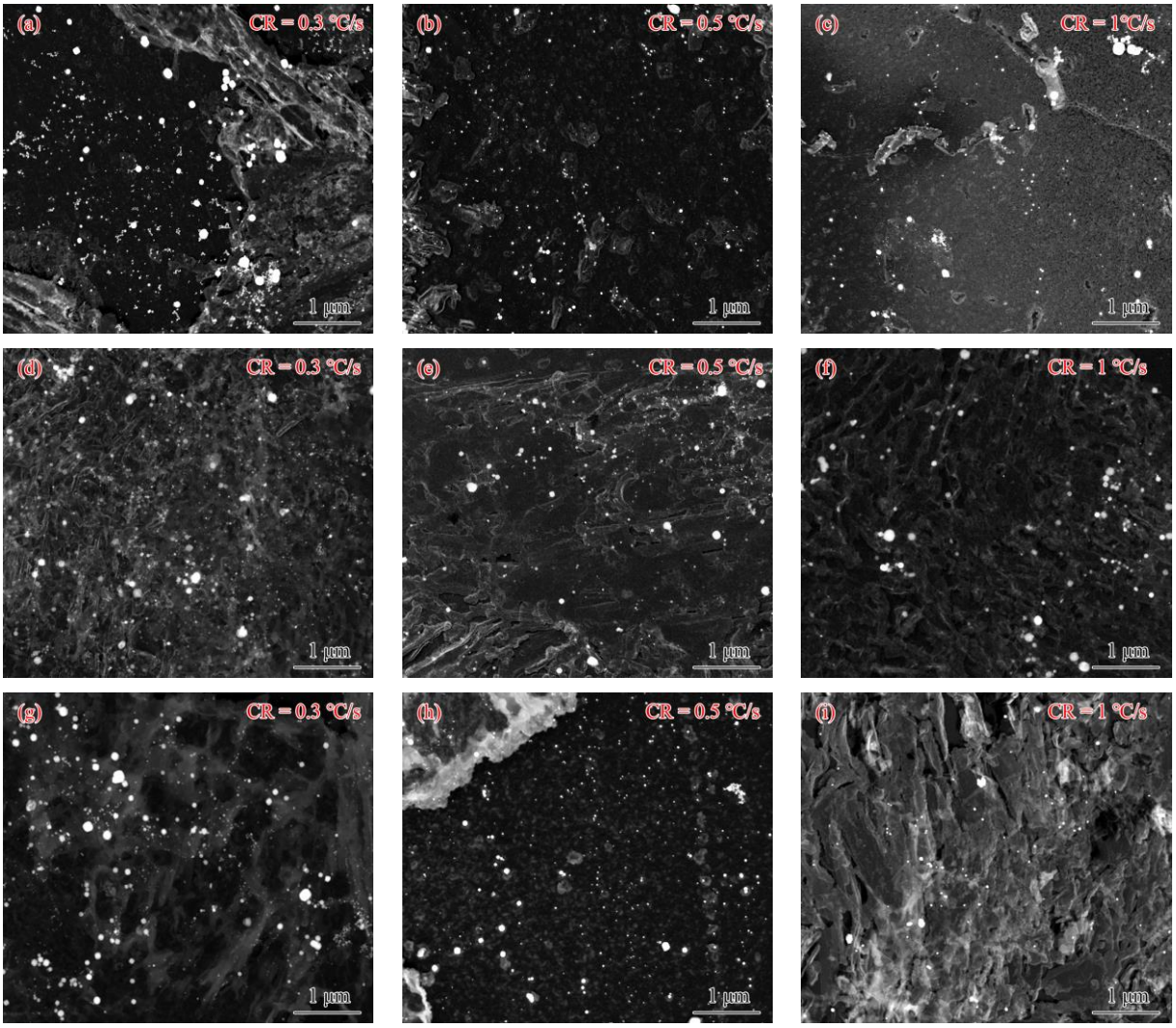

Figure 11. STEM morphology of precipitates. (**a**–**c**) Nb-1, (**d**–**f**) Nb-2 and (**g**–**i**) Nb-3.

In the equation, *YS* is the yield strength; *TS* is the tensile strength; H_{v} is the hardness of the tested steel. From this, the yield strength and tensile strength of three tested steels can be calculated. Hardness has a linear relationship with yield strength and tensile strength. The higher the hardness, the greater the strength. The yield strength of three tested steels under the cooling rate range of 0.3 to 1 °C/s is over 400MPa, the tensile strength is over 600 MPa, which properties meet the requirements of GB1499.2-2018 for HRB400E.

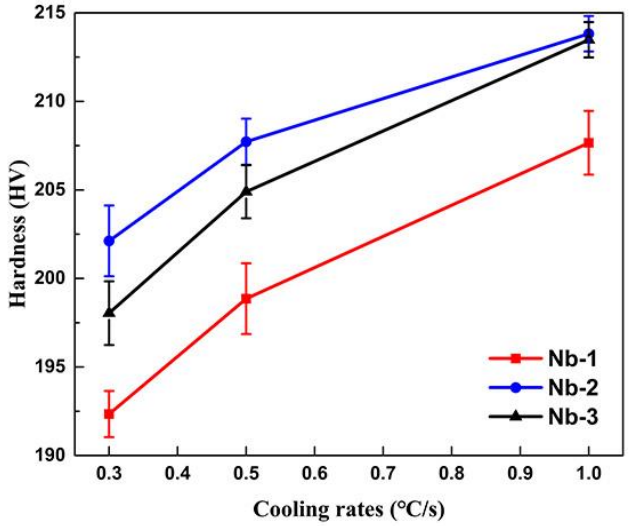

Figure 12. Dependence of hardness on cooling rate of the tested steels.

4. Discussion

4.1. Effect of Nb Solid Solution and Precipitation on Austenite Microstructures

As shown in Figure 2, the prior austenite average grain size of Nb-1 steel and Nb-2 steel are 64.84 μm and 138.63 μm, respectively, with a difference of about 70 μm. When RT decreases, the Nb-containing undissolved phases significantly increase and refines the prior austenite grains. However, after double-pass rolling, the austenite grain sizes of Nb-1 steel and Nb-2 steel are refined to 24.26 μm and 30.87 μm, respectively, and the grain size difference is only about 6 μm (as shown in Figure 3). During the whole process of austenite deformation, compared with Nb-1 steel, although Nb-2 steel has coarse prior austenite grains, the austenite grains are obviously refined after rolling, which is similar to that of Nb-1 steel. Figure 13 shows the stress-strain relationship of the tested steels in double-pass rolling. Comparing the stress-strain curves of Nb-1 steel and Nb-2 steel during the first pass of rolling, it can be seen that the curve of Nb-1 steel is a dynamic recrystallization type, and that of Nb-2 steel is a work hardening type. When the strain is 0.275, the stress of Nb-1 steel reaches its peak value. When the strain is lower than 0.275, the stress of Nb-1 steel is larger than that of Nb-2 steel, but when the strain is greater than 0.275, the situation is opposite; the stress of Nb-1 steel is lower than that of Nb-2 steel. This is because when the strain is higher than 0.275, the Nb-1 steel undergoes recrystallization, so the stress of the Nb-1 steel decreases as the strain increases. By comparing the recrystallization of pure iron and Fe-Nb alloy austenite, Maruyama et al. [27] found that solute Nb delays the recrystallization of austenite. According to research [28] on the solid solution and precipitation behavior of microalloying elements in steel, the size difference between the solute niobium atoms and iron atoms is large (r_{Nb}/r_{Fe} = 1.145). Nb-2 steel has higher solute Nb content than Nb-1 steel. There is a large lattice distortion energy in the lattice of Nb-2 steel, the solute dragging effect is significant, and the recrystallization is effectively delayed. Therefore, increasing the amount of solute niobium can be made to sufficiently delay austenite recrystallisation during rolling and effectively refine the austenite grain size after rolling.

Observing Figure 3, two kinds of austenite grain morphologies in the tested steels after rolling can be found, equiaxed and pancaked. Generally, about 950 °C is the temperature that distinguishes the austenite recrystallized zone and the non-recrystallized zone of the steel [29]. The FRT of Nb-1 steel and Nb-2 steel is 1050 °C, which is in the recrystallization zone, and the FRT of Nb-3 steel is 950 °C, which is in the incompletely recrystallized zone. Nb-1 steel and Nb-2 steel undergo dynamic recrystallization during finish-rolling at 1050 °C, so that the austenite grains after rolling are equiaxed. However, the Nb-3 steel did not undergo complete recrystallization at 950 °C, in which the austenite grains were mostly pancaked and had high deformation energy storage.

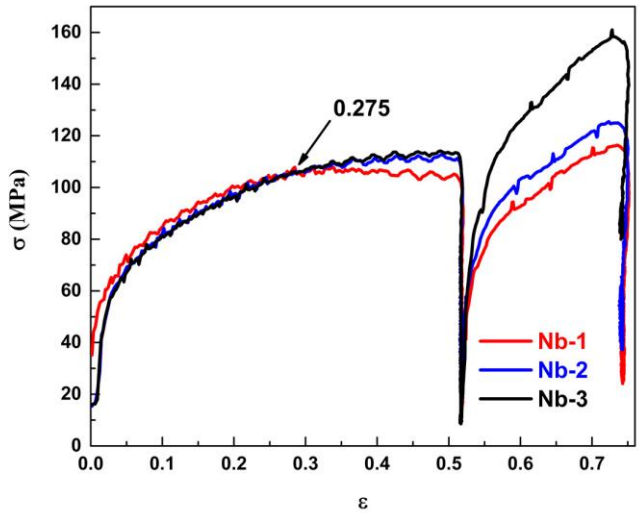

Figure 13. Stress-strain curve of double-pass rolling of tested steel.

4.2. Effect of Nb Solid Solution, Precipitation and Austenite Grain on Phase Transformation

Comparing the phase transformation microstructure of Nb-1 steel and Nb-2 steel under the CR range of 0.3 to 1 °C/s, the coarse austenite grains significantly reduce the temperature of A_{r3} and delays the occurrence of ferrite and pearlite transformations and effectively promotes the occurrence of bainite transformation. For the ferrite transformation, due to the large mismatch between Nb and Fe lattices, the solute Nb in the steel is easy to segregate to the grain boundary, reducing the energy of the grain boundary [30]. Meanwhile, the affinity of solute Nb and C atoms is large, which will reduce the activity of C and inhibit the diffusion of C atoms in the steel, which inhibiting the nucleation of ferrite [31] and the austenite-to-ferrite transformation is delayed. In addition, the Nb segregated to the phase interface will also have a strong drag on the phase boundary migration, thereby delaying the austenite-to-ferrite transformation and reducing the ferrite transformation temperature. For the pearlite transformation, Mehl [32] pointed out that the grain size of austenite affects the inoculation period (extended by enlargement) and nucleation rate of pearlite. Nb-2 steel has larger austenite grains before cooling, which increases the incubation period of pearlite and inhibits pearlite transformation. Meanwhile, the larger austenite grains before cooling make the ferrite grain coarsen after phase transformation. For the bainite transformation, the literature [25] shows that the nucleation rate of bainite has a negative exponential relationship with the third power of the interfacial energy. Due to the segregation of niobium at the grain boundary, the grain boundary energy of the system decreases. The reduction in the interface energy will significantly increase the nucleation rate of bainite and promote the bainite transformation. Therefore, the larger austenite grains and solute Nb are more prone to bainitic transformation before cooling at low CRs.

Compared with Nb-2 steel, the deformed austenite grains in Nb-3 steel can increase A_{r3} temperature, which delays the occurrence of the bainite transformation, so that only ferrite and pearlite transformations occurred in the lower CR range. The FRT of Nb-3 steel is 950 °C, which is in the incomplete recrystallization region. Deformed austenite grains can change the grain morphology of austenite before phase transformation, forming more deformation zones in the deformed austenite, increasing the nucleation position and nucleation rate of ferrite grains during the transformation of supercooled austenite to ferrite. With the decrease in the deformation temperature, the pancaked austenite grains have no time to recover and recrystallize, and most of the deformation energy storage generated by rolling remains inside the grains, which reduces the stability of the supercooled austenite [33] and the A_{r3} point is increased. Larger deformation of austenite, or deformation at lower temperatures, results in a higher density of defects (dislocations). The dislocations formed by the deformation will hinder the directional

growth of bainite, which leads to the retardation or even stops the bainite transformation. Therefore, the deformed austenite often exhibits mechanical stability during the bainite transformation, which inhibits the growth of bainite [25]. After the end of finish-rolling, the higher deformation energy storage promotes the transformation of supercooled austenite to ferrite, thereby refining the ferrite grains and increasing the transformed ferrite content. Under the CR range of 0.3 to 0.5 °C/s, C and Nb atoms have enough time to diffuse, so only ferrite and pearlite transformations occur. When the CR rises to 1 °C/s, the diffusion of C and Nb atoms is hindered, and bainite transformation can be also occur in addition to ferrite and pearlite transformation.

5. Conclusions

In this work, three kinds of niobium microalloyed high-strength anti-seismic rebars with different solute Nb and austenite microstructures were designed, and the cooling phase transformation and microstructure after rolling were studied. The following conclusions can be drawn:

(1) When the reheating temperature is lowered, the solute Nb is reduced, and the prior austenite grains are fine. When the finish-rolling temperature is reduced from 1050 °C to 950 °C, the deformed austenite grains exist. Both methods can move the dynamic CCT of 20MnSiNb steel curve to the upper left, inhibit the formation of bainite or promote the formation of ferrite and pearlite at low cooling rates, and increase the A_{r3} temperature by 20 °C and 30 °C, respectively.

(2) Increasing the content of solute Nb and deformed austenite grains can significantly increase the precipitation of Nb-containing second phases during post-rolling cooling. Precipitation strengthening and microstructure strengthening increase the hardness of the transformed microstructure after cooling, and further improve the yield strength and tensile strength of Nb-microalloyed steel.

(3) In order to obtain the F+P microstructure, niobium microalloyed high-strength anti-seismic rebars can be produced by two processes of reheating temperature of 1100 °C + finish-rolling temperature of 1050 °C or reheating temperature of 1200 °C + finish-rolling temperature of 950 °C. The post-rolling cooling rates ranged from 0.3 to 1 °C/s and 0.3 to 0.5 °C/s, respectively.

Author Contributions: Conceptualization, J.C. and X.L.; methodology, J.C. and S.Y.; validation, X.L.; formal analysis, J.C. and X.L.; investigation, X.L., J.C. and S.Y.; resources, W.C., W.Z. and J.C.; writing—original draft preparation, X.L.; writing—review and editing, X.L. and J.C.; visualization, X.L. and J.C.; supervision, X.L. and J.C.; project administration, J.C. and S.Y.; funding acquisition, Y.Z. and A.G. All authors have read and agreed to the published version of the manuscript.

Funding: This research was funded by CITIC Metal Microalloying Technical Center under grant numbers 2018530101000721.

Institutional Review Board Statement: Not applicable.

Informed Consent Statement: Not applicable.

Data Availability Statement: The raw/processed data required to reproduce these findings cannot be shared at this time as the data also forms part of an ongoing study.

Acknowledgments: Special thanks are also due to the instrumental or data analysis from Analytical and Testing Center, Kunming University of Science and Technology, China.

Conflicts of Interest: The authors declare no conflict of interest.

References

1. Lu, P.Y.; Liu, Y.; Wu, H.J. Fatigue Performance of Microalloyed high-strength rebar and analysis of fracture mechanism. *J. Iron Steel Res. Int.* **2015**, *22*, 1149–1155. [CrossRef]
2. Hui, Y.J.; Pan, H.; Liu, K.; Li, W.Y.; Yu, Y.; Chen, B.; Cui, Y. Strengthening mechanism of 600 MPa grade Nb-Ti microalloyed high formability crossbeam steel. *Acta Metall. Sin.* **2017**, *53*, 937–946.

3. Yang, C.F.; Wang, Q. Research, Development, and Production of V-N Microalloyed High Strength Rebars for Building in China. *J. Iron Steel Res. Int.* **2008**, *15*, 81–86. [CrossRef]
4. Lv, Y.K.; Zhao, X.R.; Shi, T.; Bai, L.; Liu, X.L.; Chen, J. Microstructure evolution of 400 MPa class rebar produced by QST and VNM technology under the high strain and low cycle fatigue. *Constr. Build. Mater.* **2019**, *229*, 116889. [CrossRef]
5. Sheng, X.W.; Zheng, W.Q.; Y, Y. Tensile and high-cycle fatigue performance of HRB500 high-strength steel rebars joined by flash butt welding. *Constr. Build. Mater.* **2020**, *241*, 118037. [CrossRef]
6. Cadoni, E.; Dotta, M.; Forni, D.; Tesio, N.; Albertini, C. Mechanical behaviour of quenched and self-tempered reinforcing steel in tension under high strain rate. *Mater. Des.* **2013**, *49*, 657–666.
7. Zhao, J.W.; Jiang, Z.Y.; Lee, C.S. Enhancing impact fracture toughness and tensile properties of a microalloyed cast steel by hot forging and post-forging heat treatment processes. *Mater. Des.* **2013**, *47*, 227–233. [CrossRef]
8. Musonda, V.; Akinlabi, E.T. Standard requirements of hot rolled thermo-mechanically treated reinforcement bars. *Mater. Today.* **2018**, *5*, 18593–18602. [CrossRef]
9. Dhua, S.K.; Sarkar, P.P. Development of ultrafine grains in C–Mn steel plates through hot-rolling and air-cooling. *Mater. Sci. Eng. A* **2013**, *575*, 177–188. [CrossRef]
10. Yang, W.Y.; Chen, Y.F.; Tao, Q.N.; Wang, D.X.; Zhang, H.B.; Wang, C.M. Analysis and control of abnormal band-like structure of 600 MPa seismic reinforcement steel rebar. *J. Iron Steel Res.* **2020**, *32*, 1014–1020.
11. Nikolaou, J.; Papadimitriou, G.D. Impact toughness of reinforcing steels produced by (i) the tempcore process and (ii) microalloying with vanadium. *Int. J. Impact Eng.* **2005**, *31*, 1065–1080. [CrossRef]
12. Cetinel, H.; Toparlh, M.; Özsoyeller, L. A finite element based prediction of the microstructural evolution of steels subjected to the Tempcore process. *Mech. Mater.* **2000**, *32*, 339–347. [CrossRef]
13. Shanmugam, S.; Misra, R.D.K.; Mannering, T.; Panda, D.; Jansto, S.G. Impact toughness and microstructure relationship in niobium- and vanadium-microalloyed steels processed with varied cooling rates to similar yield strength. *Mater. Sci. Eng. A.* **2006**, *437*, 436–445. [CrossRef]
14. Taca, M.; Constantinescu, D.M.; Baciu, F.; Geanta, V.; Daisa, D.; Stefanoiu, R. Influence of technological parameters on the toughness improvement of microalloyed steels. *Mater. Today.* **2016**, *3*, 1177–1182. [CrossRef]
15. Lv, Y.K.; Sheng, G.M.; Huang, Z.H. High strain and low cycle fatigue behaviors of rebars produced by QST and V-N microalloying technology. *Constr. Build. Mater.* **2013**, *48*, 67–73. [CrossRef]
16. Lv, Y.K.; Sheng, G.M.; Jiao, Y.J. Effect of V/N ratio on the high strain and low cycle fatigue behaviors of V–N microalloyed rebars. *Constr. Build. Mater.* **2014**, *69*, 18–25. [CrossRef]
17. Fang, F.; Yong, Q.L.; Yang, C.F.; Su, H. A model for precipitation kinetics in Vanadium microalloyed Steel. *J. Iron Steel Res. Int.* **2010**, *17*, 36–42. [CrossRef]
18. Huang, B.M.; Yen, H.W.; Ho, D.; Ho, H.; Yang, J.R. The influence of Widmanstätten ferrite on yielding behavior of Nb-containing reinforcing steel bars. *Scr. Mater.* **2012**, *67*, 431–434. [CrossRef]
19. Ye, Y.P.; Yin, S.B.; Gao, P.; Zhang, Y.Q.; Chen, W.; Cao, J.C. Effect of soaking temperature on austenitization and solid solution of niobium in anti-seismic rebar. *J. Iron Steel Res.* **2019**, *31*, 830–836.
20. Cao, J.C.; Ye, Y.P.; Yin, S.B.; Zhang, W.Q.; Chen, W.; Zhang, Y.Q. Deformed austenite continuous cooling transformation in Nb microalloyed anti-seismic rebar. *Iron Steel.* **2019**, *54*, 81–88.
21. Zeng, Z.Y.; Li, C.G.; Li, Z.Y.; Zhai, Y.L.; Wang, J.; Li, Z.S. Effect of Nb content and thermal deformation on the microstructure and mechanical properties of high-strength anti-seismic rebar. *Mater. Sci. Eng. A.* **2022**, *840*, 142929. [CrossRef]
22. Chen, W.; Shi, Z.; Wang, T.; Liu, H.B.; Zhang, W.Q. The reason analysis and control of lower elongation for HRB500 high-strength and anti-seismic rebars. *Mater. Rev.* **2010**, *24*, 56–59.
23. Yong, Q.L.; Pei, H.Z.; Tian, J.G.; Zhou, X.L.; Pan, L.; Yang, W.Y. Physico-metallurgical data of Niobium in steel. *J. Iron Steel Res.* **1998**, *10*, 66–69.
24. Yong, Q.L. *Second Phase in Steel Materials*; Metallurgical Industry Press: Beijing, China, 2006; p. 357.
25. Xu, Z.Y. Effect of stress on bainitic transformation in steel. *Acta Metall. Sin.* **2004**, *40*, 113–119.
26. Pavlina, E.J.; Van Tyne, C.J. Correlation of yield strength and tensile strength with hardness for steels. *J. Mater. Eng. Perform.* **2008**, *17*, 888–893. [CrossRef]
27. Maruyama, N.; Smith, G.D.W. Effect of nitrogen and carbon on the early stage of austenite recrystallisation in iron-niobium alloys. *Mater. Sci. Eng. A.* **2002**, *327*, 34–39. [CrossRef]
28. Zhang, Z.Y.; Sun, X.J.; Yong, Q.L.; Li, Z.D.; Wang, Z.Q.; Wang, G.D. Precipitation behavior of nanometer-size carbides in Nb-Mo microalloyed high strength steel and its strengthening mechanism. *Acta Metall. Sin.* **2016**, *52*, 410–418.
29. Huang, M.; Cao, J.C.; Chen, W.; Zhou, X.L.; Yang, Y.H.; Zhong, Z.H. Effects of deformation conditions on dynamic recrystallization of a Nb microalloyed anti-seismic rebar. *J. Donghua Uni. (Eng. Ed.)* **2015**, *32*, 879–886.
30. Dong, H.K.; Zhang, Y.J.; Miyamoto, G.; Inomoto, M.; Chen, H.; Yang, Z.G.; Furuhara, T. Unraveling the effects of Nb interface segregation on ferrite transformation kinetics in low carbon steels. *Acta Mater.* **2021**, *215*, 117081. [CrossRef]
31. He, X.L.; Yang, G.W.; Mao, X.P.; Yu, C.B.; Da, C.L.; Gan, X.L. Effect of Nb on the continuous cooling transformation rule and microstructure, mechanical properties of Ti-Mo bearing microalloyed steel. *Acta Metall. Sin.* **2017**, *53*, 648–656.

32. Hull, F.C.; Colton, R.A.; Mehl, R.F. Rate of nucleation and rate of growth of pearlite. *Trans. AIME.* **1942**, *50*, 185.
33. Li, L.; Ding, H.; Yang, C.Z.; Du, L.X.; Liu, X.H.; Wang, G.D.; Song, H.M. Effect of controlled rolling and controlled on microstructure and mechanical properties of low carbon steel microalloyed with Nb. *J. Iron Steel Res.* **2006**, *18*, 46–51.